Rotating bouncing disks, tossing pizza dough, and the behavior of ultrasonic motors

Kuang-Chen Liu, James Friend, and Leslie Yeo

MicroNanophysics Research Laboratory, Department of Mechanical Engineering, Monash University, Victoria 3800, Australia

Pizza tossing and certain forms of standing-wave ultrasonic motors (SWUMs) share a similar process for converting reciprocating input into continuous rotary motion. We show that the key features of this motion conversion process such as collision, separation and friction coupling are captured by the dynamics of a disk bouncing on a vibrating platform. The model shows that the linear or helical hand motions commonly used by pizza chefs and dough-toss performers for *single tosses* maximize energy efficiency and the dough's airborne rotational speed; on the other hand, the semielliptical hand motions used for *multiple tosses* make it easier to maintain dough rotation at the maximum speed. The system's bifurcation diagram and basins of attraction also provide a physical basis for understanding the peculiar behavior of SWUMs and provide a means to design them. The model is able to explain the apparently chaotic oscillations that occur in SWUMs and predict the observed trends in steady-state speed and stall torque as preload is increased.

I. INTRODUCTION

Like many nonlinear dynamical systems, the seemingly simple equations that govern a ball bouncing on a vibrating platform under a constant gravitational field describe very complex behavior. A variety of interesting phenomena accompany the bouncing ball system, including noise-sensitive hysteresis loops [1], period doubling route to chaos, and eventually periodic orbits known as the "sticking solution," or "complete chattering" [2,3]. Due to its physical simplicity and rich nonlinear behavior, the system has found a variety of applications, from the dynamics of two-dimensional granular gases [4], high energy ball milling [5], to its use as a pedagogical demonstration of chaos [6].

Regardless of the various complex bouncing dynamics that it displays, the response of the traditional bouncing ball system is ultimately an oscillatory one: the mean vertical velocity is zero, and, as long as the collision is not perfectly elastic, the displacement of the ball is bounded. However, through a simple extension of the system by adding a rotational degree of freedom and an angular component to the platform vibration, a different set of phenomena is made possible: stick-slip rotation while the disk and platform are in contact, impulsive frictional torque imparted at each collision, and the potential for nonzero mean angular velocity and unbounded rotary motion.

This process of motion transfer—the conversion of reciprocating motion into continuous rotary motion in the modified system—is intimately related to pizza tossing and the stator-rotor interaction in a class of standing-wave ultrasonic motors (SWUMs) [7–9]. As illustrated in Fig. 1, the system may be represented as a *disk* or a *pizza dough* with angular α and linear x displacements, bouncing on an oscillating *platform* or a pair of *dough-tossing hands* with a combined angular β and linear oscillation s described by

$$\beta(t) = \Phi \sin(\omega t + \theta) \quad \text{and} \quad s(t) = A \sin(\omega t). \quad (1)$$

Figure 2 shows a family of potential trajectories traced by a dough-tossing hand or a SWUM stator as the amplitude ratio

$L = a_e \Phi / A = \tan \phi_L$ and phase lag θ are varied (a_e is the effective friction contact radius).

Of the many different hand trajectories that may be used to toss a pizza, we observe that distinct hand motions are used in two different dough-tossing modes. In the first mode [10], the dough begins each cycle at rest relative to the hand: the dough is launched, caught upon its descent, allowed to come to rest, and the process is repeated. Since each toss begins with the same initial conditions, the process can be considered as a chain of *single tosses*. In this case, we observe that a linear trajectory resembling Fig. 2(c) is employed. In the second mode [11], the dough is not allowed to come to rest after each collision, and thus the rotation of the dough is maintained over *multiple tosses*. In this case, the tossing motion traces a semielliptical trajectory resembling Fig. 2(b).

One of our key goals in this paper is to investigate why the particular hand motions are adopted by dough-tossing performers for the two dough-tossing modes. Do these hand
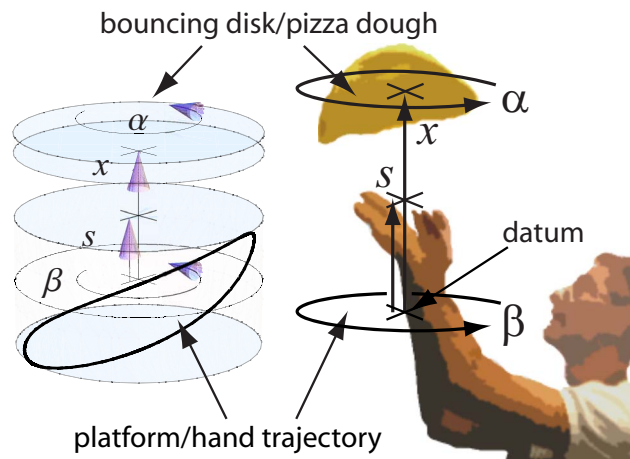

FIG. 1. (Color online) The displacement variables of the bouncing-disk system and pizza tossing. The trajectories traced by a point on the oscillating platform and a dough-tossing hand are given by Eqs. (1), which describe a family of closed curves on the surface of a cylinder.
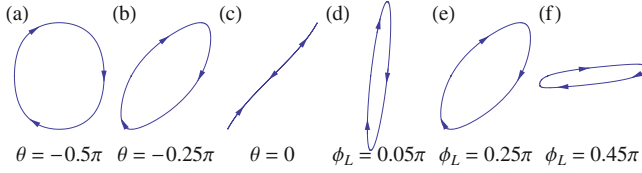
FIG. 2. (Color online) Potential dough-tossing motions and SWUM stator trajectories: (a)–(c) the effect of varying phase lag θ with $\phi_L = \pi/4$, and (d)–(f) the effect of varying amplitude ratio $L = \tan(\phi_L)$ with $\theta = -\pi/4$.

motions provide any advantages in terms of the effort required, the rotary speed reached by the dough, and ease of handling? Noting that the operation of SWUMs can be seen as a continuous sequence of multiple pizza tosses, answers to the above questions about pizza tossing—originally conceived as merely a pedagogical tool—will also help us better understand the underlying motion transfer process in SWUMs: the generation of continuous rotation from an oscillatory input.

A number of attempts have been made to model SWUMs over the years [7,12,13], however, these models have so far assumed that the vertical motion of the rotor is negligible. This assumption may be valid when the rotor preload dominates over the inertial force of the stator acceleration and the rotor operates in the nonbouncing regime. More precisely, in terms of the dimensionless forcing parameter $\Gamma = A\omega^2/\pi g$, where g is the rotor acceleration due to preload, the rotor will remain in contact with the stator when $\Gamma < 1/\pi$. However, most motors operate with $\Gamma > 1/\pi$. For example, our SWUM [8] operating at 70 kHz with the rotor under gravitational acceleration has a lower estimate of $\Gamma \approx 6$ if we assume a stator vibration of merely 1 nm; Tsujino's SWUM [14] with a stator vibration of 5 μm at 55 kHz and a rotor under a preload acceleration of 9×10^3 m/s^2 has $\Gamma \approx 70$. As will be shown, the bouncing-disk model reproduces key qualitative features of the motor's dynamics, including the seemingly chaotic oscillations of the rotor's transient speed curves and the effect of preload on steady-state speed and stall torque.

The structure of the current paper is as follows: in Sec. II we describe details of our bouncing-disk model; in Sec. III we use our model to investigate the optimal hand motion for single tosses; in Sec. IV we investigate the best way to maintain dough rotation over multiple tosses and its implication for SWUMs by considering how various bouncing-disk orbits (e.g., periodic, chaotic, or chattering) and their basins of attraction affect the motion transfer process; and in Sec. V, we compare our model's predictions with results from a prototype motor, showing that the bouncing-disk model is able to account for important SWUM characteristics that could not be explained by existing models.

Note that we neglect dough deformation in this paper for the following reasons: (1) our focus is on pizza tossing as a method for imparting rotary motion rather than dough shaping, (2) the typical rate of dough deformation is low ($\sim 3\%$ increase in diameter per toss, see Appendix), and (3) pizza tossing is used as a pedagogical tool for understanding the rotor dynamics in SWUMs. Dough plasticity only has a minor effect on the dynamics and will not be considered further

here. Although we assume that the rotor of SWUM is under constant preload, our model would still be valid for sprung rotors if the spring (with stiffness k) operates purely in compression and the spring's mean displacement δl_0 is much greater than the rotor's peak-to-peak displacement amplitude. Under such conditions, the spring force is effectively constant and the rotor's acceleration due to the spring preload is given by $g = k\delta l_0/m$.

In a previous publication [15], we have briefly reported the application of the bouncing-disk model to pizza tossing, and its potential implications for SWUMs. In this paper, we provide the full details for the modeling of single and multiple pizza tosses, and we make an in-depth comparison between our theoretical predictions and the experimental results of SWUMs.

II. THE BOUNCING-DISK MODEL

A. Equations of motion

As an extension of the traditional bouncing ball problem, the vertical component of the bouncing-disk system has the same assumptions and governing equations as previous work [3]: collisions have zero duration and the coefficient of restitution ϵ is independent of the impact velocity. For the rotary component, we assume that the contact pressure is uniform and that the frictional torque can be modeled using Coulomb friction with a constant coefficient of friction μ acting at an effective contact radius a_e (we assume that the kinetic and static coefficients of friction are equal). The resulting governing equations for the motion of the disk are

$$ma_g^2\ddot{\alpha} = T_f + \sum_{n=1}^{\infty} \hat{H}_n \delta(t - t_n), \tag{2a}$$

and

$$m\ddot{x} = -mg + N + \sum_{n=1}^{\infty} \hat{F}_n \delta(t - t_n), \tag{2b}$$

where N is the normal contact force, T_f is the frictional torque, $\hat{F}_n$ and $\hat{H}_n$ are the linear and angular impulse at time t_n from the disk's nth collision with the platform, δ is the Dirac delta function, m is the disk's mass, and a_g is the radius of gyration. The platform displacements (s, β) prescribed by Eqs. (1) enters Eqs. (2) through the following forcing terms: N, T_f, $\hat{F}_n$, and $\hat{H}_n$; their functional forms are described below.

During the contact phase, the normal contact force N assumes a value such that $x = s$. However, in the absence of adhesion forces N must remain non-negative; thus the rotor and the stator separates if N falls to zero when $\ddot{s} \leq -g$. The functional form of N is then

$$N = \begin{cases} 0, & \ddot{s} \leq -g \text{ or } x \neq s \\ m(g + \ddot{s}), & \ddot{s} > -g \text{ and } x = s \end{cases}. \tag{3}$$

Depending on the normal contact force N, the relative angular velocity $\dot{\alpha} - \dot{\beta}$ and the angular acceleration $\ddot{\beta}$ of the stator, the torque acting on the rotor can arise from either

static or kinetic friction. When the sliding speed is zero ($\dot{\alpha} - \dot{\beta} = 0$) and the angular acceleration $\ddot{\beta}$ is within (or entering) the static friction envelope $S_{env} = \{\ddot{\beta}: |\ddot{\beta}| < \ddot{\beta}_{env}\}$ (where $\ddot{\beta}_{env} = \mu a_e N / m a_g^2$), the frictional torque is static and it exactly balances the rotor's inertia so that $\alpha = \beta$. If the sliding speed is nonzero ($\dot{\alpha} - \dot{\beta} \neq 0$), or the angular acceleration is outside (or exiting) the static friction envelope, then the frictional torque is kinetic and it acts to oppose the sliding motion. The above description is partially summarized by the following equation:

$$T_f = \begin{cases} ma_g^2 \ddot{\beta}, & \dot{\alpha} = \dot{\beta} \text{ and } \ddot{\beta}_{env} > |\ddot{\beta}| \\ \mu a_e N, & \dot{\alpha} = \dot{\beta} \text{ and } \ddot{\beta}_{env} < \ddot{\beta} \\ -\mu a_e N, & \dot{\alpha} = \dot{\beta} \text{ and } -\ddot{\beta}_{env} > \ddot{\beta} \\ -\mu a_e N \operatorname{sgn}(\dot{\alpha} - \dot{\beta}), & \dot{\alpha} \neq \dot{\beta} \end{cases} , \tag{4}$$

where sgn is the signum function.

The axial impulse of the nth collision $\hat{F}_n$ is given by

$$\hat{F}_n = \int_{t_n^-}^{t_n^+} F(t) dt = m(\dot{x}^+ - \dot{x}^-), \tag{5}$$

where the superscripts $(-, +)$ are used to denote, respectively, a quantity before and after the collision. Since we are modeling the collision with a speed-independent coefficient of restitution ϵ, the relationship between the preimpact and postimpact relative vertical velocity is

$$\dot{s} - \dot{x}^+ = -\epsilon(\dot{s} - \dot{x}^-). \tag{6}$$

Substituting Eq. (6) into Eq. (5), we obtain the expression for the nth axial impulse

$$\hat{F}_n = m(\dot{x}^+ - \dot{x}^-) = m(1 + \epsilon)(\dot{s} - \dot{x}^-). \tag{7}$$

The determination of the frictional impulse $\hat{H}_n$ requires consideration of the "available" impulse $\hat{H}_{n,a}$ and the maximum "possible" impulse $\hat{H}_{n,p}$. The available impulse $\hat{H}_{n,a}$ is the torsional impulse that would be transmitted if sliding friction were present over the whole collision

$$\hat{H}_{n,a} = -\int_{t_n^-}^{t_n^+} \mu a_e \operatorname{sgn}(\dot{\alpha} - \dot{\beta}) F(t) dt = -\mu a_e \operatorname{sgn}(\dot{\alpha}^- - \dot{\beta})\hat{F}_n. \tag{8}$$

Note that the frictional torque may only be present over a fraction of the collision, vanishing when the relative angular velocity between the rotor and the stator is reduced to zero (static friction is ignored since the collision is short). If a cap is not imposed on $\hat{H}_n$, scenarios where the relative rotation of the rotor reverses direction after impact would occur. The maximum transferable impulse is thus limited to the amount that would result in $\dot{\alpha}^+ - \dot{\beta} = 0$, which is

$$\hat{H}_{n,p} = -ma_g^2(\dot{\alpha}^- - \dot{\beta}), \tag{9}$$

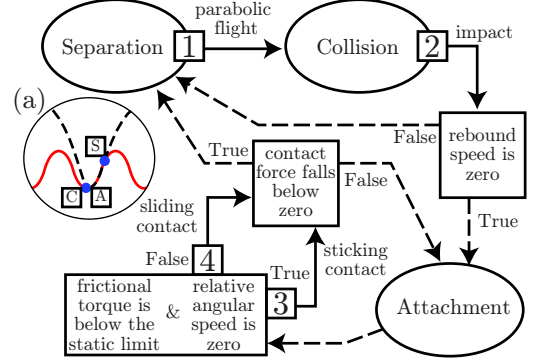and the frictional angular impulse is given by

FIG. 3. (Color online) Model simulation flow chart. The inset (a) shows a potential trajectory of the bouncing disk (dashed line) and the oscillating platform (solid line) for one cycle of simulation, starting with collision (c), attachment (a), and ending with separation (s).

$$\hat{H}_n = \begin{cases} \hat{H}_{n,a}, & \text{if } |\hat{H}|_{n,a} \leq |\hat{H}|_{n,p} \\ \hat{H}_{n,p}, & \text{if } |\hat{H}|_{n,p} < |\hat{H}|_{n,a} \end{cases} . \tag{10}$$

B. Method of solution

Except for gravity, the forces experienced by the bouncing disk are all associated with some form of discontinuity: the impulsive forces ($\hat{F}_n, \hat{H}_n$) cause sharp changes to the disk's velocity, the contact force can only support compressional loads ($N \not< 0$), and the frictional torque can switch between static and kinetic friction and has a jump discontinuity when relative sliding velocity changes sign $[-\mu a_e N \operatorname{sgn}(\dot{\alpha} - \dot{\beta})]$. The result of these discontinuities is that the disk described by Eq. (2) experiences four distinct phases: (1) parabolic flight, (2) impact, (3) sticking contact, and (4) sliding contact, each of which may be solved analytically. The following paragraph outlines how the four phases are sequenced as a solution to Eq. (2) and the whole process is summarized in Fig. 3.

During parabolic flight, gravity is the only acting force so that $x(t) = x_n + v_n(t - t_n) - \frac{g}{2}(t - t_n)^2$ and $\dot{\alpha}(t) = \dot{\alpha}_n$. The phase ends when the disk collides with the platform, where the time of collision is determined by solving for t_{n+1} such that $x(t_{n+1}) = s(t_{n+1})$

$$x_n + v_n(t_{n+1} - t_n) - \frac{g}{2}(t_{n+1} - t_n)^2 = A \sin(\omega t_{n+1}). \tag{11}$$

After determining the postimpact velocities through Eqs. (6) and (10), if the rebound speed $\dot{x} - \dot{s}$ is zero and the contact force is positive $N > 0$, the system enters one of two contact phases, otherwise the disk is relaunched into parabolic flight. The two contact phases differ in terms of whether the friction is static or kinetic. If the disk satisfies the condition described in Eq. (4) for static friction, then $\dot{\alpha} = \dot{\beta}$; otherwise, the system undergoes sliding contact and the angular rotation of the disk is determined by solving

TABLE I. Full specification of a single toss

θ (rad)	ϕ_L (rad)	c (m)	ω (rad/s)	a_e (m)	a_g (m)	μ	g (m/s)
0	0.55 ± 0.14	0.25 ± 0.05	15 ± 5	0.135 ± 0.015	0.11 ± 0.01	0.6 ± 0.1	9.8

$$ma_g^2\ddot{\alpha} = -\mu a_e N \, \mathrm{sgn}(\dot{\alpha} - \dot{\beta}). \tag{12}$$

The two contact phases switch between each other according to the following conditions: stick changes to slip if the platform's angular acceleration exceeds the static friction limit, and slip changes to stick if the sliding speed reaches zero. Both contact phases end when N falls to zero and the disk is launched into parabolic flight.

III. SINGLE TOSSES OF PIZZA DOUGH

A. Performance measures and parameters

We simulate our bouncing-disk model for a single launch cycle to investigate what the best hand motion is for single tosses as θ and L are varied. To compare the different tossing motions, the following performance measures are used: (1) the airborne rotational speed $\dot{\alpha}_f$ reached by the pizza dough, (2) the energy efficiency η or ratio of the rotational kinetic energy gained by the dough over the total energy input due to the tossing motion, and (3) the speed ratio ν of the dough's airborne angular velocity $\dot{\alpha}_f$ over the maximum rotary tossing speed $\omega\Phi$.

Noting that the amplitude ratio $L = \tan\phi_L = a_e\Phi/A$, and that the arc length of the linear dough-tossing trajectory $c = \sqrt{A^2 + (a_e\Phi)^2}$, we can express A and Φ as functions of ϕ_L and c

$$(a_e\Phi, A) = c(\sin\phi_L, \cos\phi_L). \tag{13}$$

Specifying (A, Φ) in terms of (c, ϕ_L) has the following advantages: by keeping c constant, the stroke length of the dough-tossing motion remains bounded as we vary the amplitude ratio L, and by varying ϕ_L between 0 and $\pi/2$ all possible L from 0 to ∞ are explored.

The full specification of a single toss in our bouncing-disk model can be determined by the following set of independent parameters: θ, ϕ_L, c, ω, a_e, a_g, μ, and g. Initial conditions

and the coefficient of restitution are not part of the specification because we are only concerned with a single launch cycle and the dough always begins each toss at rest with $t_0 = 3T/4 = 3\pi/2\omega$ (i.e., the lowest point of the tossing motion). The parameter values we use in this investigation are shown in Table I). The coefficient of friction between skin and dough is estimated to be $\mu = 0.6 \pm 0.1$ through the inclined plane test (a baked bread begins to slip on a lightly floured hand at a slope of $30° \pm 5°$); the gravitational acceleration $g = 9.8$ m/s^2. The rest of the parameters are based on a video of pizza tossing recorded at a local pizza shop [10]: θ, a_e, a_g, and c are estimated by visual inspection; ϕ_L and ω, however, are determined from the estimated vertical and angular launch speeds: $\dot{x}_{sep} = 3.1 \pm 0.3$ m/s and $\dot{\alpha}_{sep} = 14 \pm 1.5$ rad/s. Assuming that there is no slip between the dough and the hands,

$$\dot{x}_{sep} = c\omega\cos\phi_L \quad \text{and} \quad \dot{\alpha}_{sep} = c\omega\sin\phi_L/a_e,$$

ω and ϕ_L are thus given by

$$\omega^2 = \left(\frac{\dot{x}_{sep}}{c}\right)^2 + \left(\frac{\dot{\alpha}_{sep}a_e}{c}\right)^2 \tag{14}$$

and

$$\phi_L = \tan^{-1}\left(\frac{a_e\dot{\alpha}_{sep}}{\dot{x}_{sep}}\right).$$

B. Results and discussion

The effects of varying the amplitude ratio ϕ_L and the phase lag θ are shown in Figs. 4(a)–4(c). For clarity, we only show the results for $0 \le \theta \le \pi$ since $\dot{\alpha}_f$, ν, and η all possess some form of translation symmetry: for $\dot{\alpha}_f$ and ν, $f(\theta+\pi) = -f(\theta)$, and for η, $f(\theta+\pi) = f(\theta)$. We have also limited the domain of ϕ_L to $[0, \cos^{-1}(g/c\omega^2)]$ rather than the full range of $[0, \pi/2]$ because the vertical force exerted by the tossing
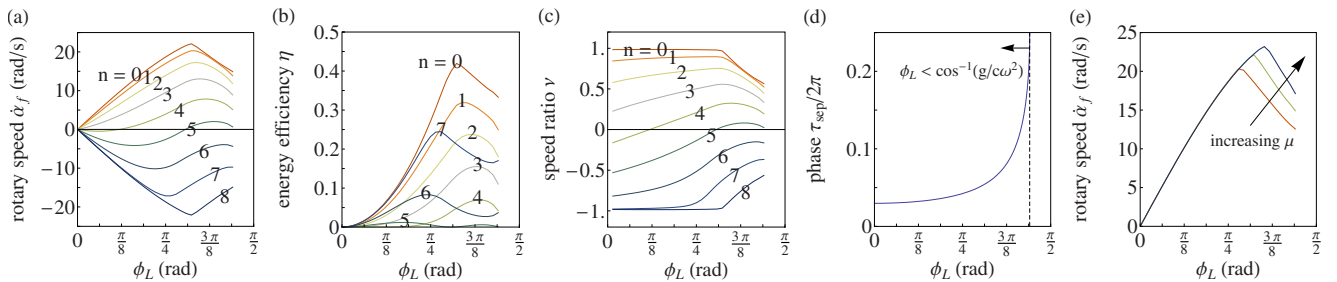

FIG. 4. (Color online) The performance of different pizza tossing techniques—as measured by (a) dough rotation speed $\dot{\alpha}_f$, (b) energy efficiency η, and (c) dough-to-hand speed ratio ν—when the amplitude ratio ϕ_L is varied at a phase lag of $\theta = n\pi/8$. (d) $\dot{\alpha}_f$ is the dough rotation speed at the phase of separation τ_{sep}, which is a function of ϕ_L with a range of $[\sin^{-1}(g/c\omega^2), \pi/4]$. (e) The effect of μ on $\dot{\alpha}_f$; the maximum $\dot{\alpha}_f$ occur at greater ϕ_L as μ is increased (0.5, 0.6 and 0.7 for the three curves).

TABLE II. Effects of input parameter uncertainties

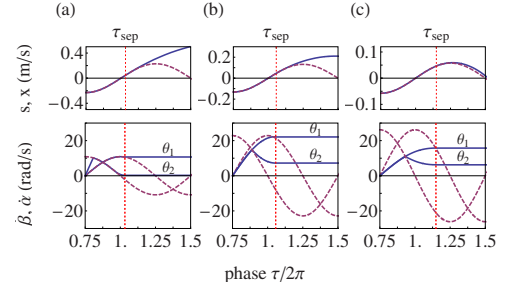| $\dot{\alpha}_f$ (rad/s)	Uncertainties (rad/s) due to					
	c	ω	a_e	a_g	μ	ϕ_L
14	± 3	± 5	± 2	± 0.01	± 0.01	± 3

FIG. 5. (Color online) Details of various hand motions (dashed curves) and the resulting dough trajectories (solid curves). Two trajectories with different phase lags ($\theta_1 = 0$ and $\theta_2 = \pi/2$) are shown for each of the following amplitude ratios ϕ_L: (a) 0.132π, (b) 0.323π, and (c) 0.426π. The effect of choosing a suboptimal ϕ_L, such as slip at high ϕ_L, and low hand rotation rate $\omega\Phi$ at low ϕ_L, can be seen by comparing the trajectories in (a) and (c) with the optimal trajectory with $\phi_L = 0.323\pi$ in (b).

motion is insufficient for overcoming gravity when $\phi_L > \cos^{-1}(g/c\omega^2)$, which means the dough never leaves the hand.

Though our model is simple, the essential physics of the torque transfer process in pizza tossing are included. The predicted dough rotation speed is 14 ± 5 rad/s for the single toss specified by Table I, which is in good agreement with the average airborne angular speed of 14 ± 1.5 rad/s in the first four pizza tosses of the video footage [10]. The effects of the uncertainties in the input parameters to our model are shown in Table II.

From Figs. 4(a)–4(c), we can see that the optimal parameters are $\theta = 0$ or π, and $\phi_L = 0.323\pi$ ($L = 1.6$), where the maximum airborne speed $|\dot{\alpha}_f| = 22$ rad/s and energy efficiency $\eta = 0.42$ are reached; the speed ratio at these points $|\nu| = 0.97$ have a negligible difference from $\max |\nu| = 0.99$ at $(\phi_L, \theta) = (0.132\pi, 0)$. The optimal hand motions predicted by our bouncing-disk model are linear trajectories with $\theta = 0$ [as shown in Fig. 2(c)], which are precisely the motions we observe in actual pizza tossing. We note, however, that there is a significant difference between the optimal $\phi_L = 0.323\pi$ predicted by our model and the observed $\phi_L = 0.175\pi \pm 0.045\pi$. We will first explain why $(\phi_L, \theta) = (0.323\pi, 0)$ is optimal in our model before returning to discuss this discrepancy.

When the contact force and the coefficient of friction are sufficiently large, the airborne rotation speed of the dough will be the same as the rotation speed of the tossing motion at the point of separation (when $\ddot{s}$ falls below $-g$). In terms of the nondimensional phase $\tau = \omega t$, the point of maximum hand rotation speed $\tau_{\max|\dot{\beta}|}$ and the point of separation τ_{sep} are, respectively, given by

$$\tau_{\max|\dot{\beta}|} = -\theta + n\pi, \quad \text{where } n = 0, 1 \ldots$$

$$\text{and} \quad \tau_{\text{sep}} = \sin^{-1}(1/\pi\Gamma). \quad (15)$$

The amplitude ratio ($\tan\phi_L = a_e\Phi/A$) affects three things: the point of separation τ_{sep} [see Fig. 4(d)], the maximum hand rotation speed $\omega\Phi$, and the normal contact force $N = m(g + \ddot{x})$; the phase lag, on the other hand, controls the point at which the maximum hand rotation speed occurs $\tau_{\max|\dot{\beta}|}$. If we let $\phi_L \to \pi/2$, we increase the hand rotation speed $\omega\Phi$, however the dough will be sliding at τ_{sep} due to reduced normal contact force; if we let $\phi_L \to 0$, there will be little rotary hand motion (compare the three columns in Fig. 5). The optimal amplitude ratio $\phi_L = 0.323\pi$ thus results from the compromise between the goal of minimizing slip and the goal of maximizing $|\dot{\beta}|$. The optimal phase lag $\theta = 0$, on the other hand, results from the balance between the torque transmitted at the beginning (τ_0) and the end (τ_{sep}) of the contact phase. If $\theta > 0$, $\tau_{\max|\dot{\beta}|}$ is shifted away from τ_{sep} to the left and thus the torque is reduced as we approach separation; if $\theta < 0$, $\tau_{\max|\dot{\beta}|}$ is shifted toward τ_{sep} on the right but there would initially be reverse torque at τ_0.

Our model suggests that the linear hand motions observed in the single toss video ($\theta = 0$) are chosen to maximize dough rotation and energy efficiency. However, the observed amplitude ratio $\phi_L = (0.175 \pm 0.045)\pi$ is much lower than the optimal value of $\phi_L = 0.323\pi$ predicted by our model, which may be caused by other factors that influence the choice of the amplitude ratio ϕ_L. For example, a dough-toss performer may be aiming for a particular toss height which requires a smaller ϕ_L (see Fig. 5) for the effect of ϕ_L on toss height. Furthermore, Fig. 4(e) shows that the optimal ϕ_L shifts toward zero as μ decreases. Since the coefficient of friction depends on the amount of dry flour present on the hands—a factor difficult to control—a dough toss performer may thus choose a low ϕ_L to minimize slip.

IV. MULTIPLE TOSSES OF PIZZA DOUGH AND SWUM BEHAVIOR

In this section we investigate the underlying motion transfer process that applies to both SWUMs and multiple pizza tosses. We will thus refer to both the pizza dough and the SWUM rotor as the *disk*, and both the dough-tossing hand and the SWUM stator as the *platform*.

Most of the angular momentum transfer between the platform and the disk occurs during impact. Much information about the motion transfer process can thus be gained by studying the "next collision" map of the bouncing-disk system: the location of attracting orbits will affect the steady-state rotation speed, and the size of their basins of attractions will affect the sensitivity of SWUMs to perturbations and the ease at which multiple pizza tosses may be executed. The following state variables are used in our next collision map: the relative axial collision velocity $w_A = \dot{x} - \dot{s}$, the relative angular collision velocity $w_T = \dot{\alpha} - \dot{\beta}$, and the phase at impact $\tau_{\text{imp}} = \omega t_{\text{imp}}$. The nondimensionalized form of the map has four parameters: Γ, ϵ, θ as previously defined, and an angular
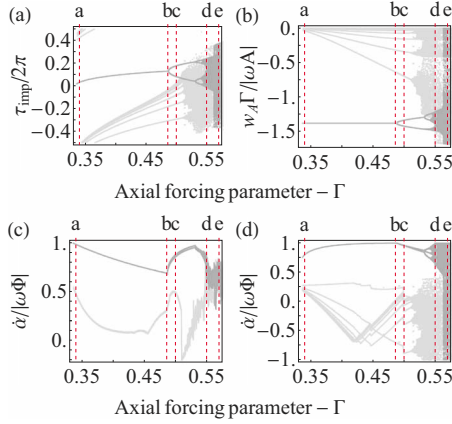
FIG. 6. (Color online) Bifurcation diagrams ($\epsilon=0.5$) showing period doubling routes to chaos (dark gray) and the evolution of the chattering mode (light gray) as Γ is increased for: (a) the phase of impact τ_{imp}, (b) the relative vertical collision speed, (c)–(d) the normalized angular collision speed when (c) $(\theta, \Gamma_T)=(0, 100)$ and (d) $(\theta, \Gamma_T)=(-0.26\pi, 1)$. Note that ϕ_L is not fixed. The basins of attraction at (a)–(e) are shown in Fig. 7. The axial forcing parameter Γ_n at the first five bifurcation points are 0.486, 0.531, 0.5402, 0.5421, and 0.5425. The ratio $\frac{\Gamma_n - \Gamma_{n-1}}{\Gamma_{n+1} - \Gamma_n}$ of the distance between the first few bifurcation points are 4.891, 4.842, and 4.750, which approaches the Feigenbaum constant 4.669…

forcing parameter $\Gamma_T = a_g^2 \Phi \omega^2 / a_e \pi g \mu$ that can be interpreted as the ratio of the inertial torque to the frictional torque due to the rotor preload. In the next two sections we will discuss the implications of the system's bifurcation plots and basins of attraction on pizza tossing and SWUMs.

A. Bifurcation diagram

The use of Coulomb friction in our bouncing-disk model means that the angular component of the disk is affected by its vertical motion but not vice versa. The governing equation for the vertical component of our bouncing-disk system is thus identical to the traditional bouncing ball system. We plot the bifurcation diagram for $\epsilon=0.5$ by "following" the period 1 attractor [16] at $\Gamma=0.335$, which undergoes a period doubling route to chaos as Γ is increased. The resulting bifurcation diagram for τ_{imp}, shown in Fig. 6(a), is consistent with Tufillaro's [2].

Also shown in Fig. 6 is the evolution of the chattering orbit, which coexists with the periodic orbit as a separate attractor in the phase space. A key feature of the chattering orbit is the occurrence of rapid collisions with decaying impact velocity and flight duration. In the idealized bouncing-disk system, it is possible for the disk to come to rest on the platform after completing an infinite number of collisions in finite time; to avoid this computational supertask [17], we artificially set w_A to zero if the impact speed is small ($|w_A \Gamma / \omega A| < 10^{-6}$) or if there are 20 consecutive short duration flights ($\tau/2\pi < 10^{-4}$). Although the complexity of the chattering orbits grows as Γ is increased, they still appear to be eventually periodic. For $\Gamma < 0.52$, the chattering orbits follow a pattern similar to those of single pizza tosses: following a long toss, the dough comes to rest on the hand

during the chattering phase and the process is repeated. On the other hand, the periodic orbits better match the dynamics of the multiple pizza tosses, and will thus be the focus of our discussion.

Since the frictional angular impulse $\hat{H}_n$ acts always to reduce the relative angular impact speed $|w_T|$ between the disk and the platform, w_T will eventually be zero for any period 1 orbit. That is,

$$\dot{\alpha}_{\mathrm{p1,ss}} = \dot{\beta}(t_{\mathrm{imp}}) = \omega \Phi \cos(\tau_{\mathrm{imp}} + \theta), \qquad (16)$$

where $\dot{\alpha}_{\mathrm{p1,ss}}$ is a period 1 steady-state dough rotational velocity, and $\dot{\beta}(t_{\mathrm{imp}})$ is the platform rotation velocity at impact. The maximum steady-state rotational speed $\dot{\alpha}_{\mathrm{p1,ss}} = \omega \Phi$ will be achieved if $\theta = -\tau_{\mathrm{imp}}$. In Fig. 6(a), we can see that period 1 orbits occur for $1/3 < \Gamma < 0.486$, and the phase of impact $\tau_{\mathrm{imp}}/2\pi$ starts at 0 and shifts to 0.130 at the first point of bifurcation, thus the stator motion needed to achieve the maximum rotation velocity can vary from a linear to a semielliptical trajectory depending on Γ.

For example, a linear trajectory with $\theta=0$ would give the maximum rotation speed $\dot{\alpha}_{\mathrm{p1,ss}} = \omega \Phi$ when $\Gamma=1/3$ and decrease to $\alpha_{\mathrm{p1,ss}} = \omega \Phi \cos(0.26\pi)$ when $\Gamma=0.486$, as shown in the bifurcation diagram of $\dot{\alpha}/|\omega\Phi|$ for $(\theta, \Gamma_T)=(0, 100)$ in Fig. 6(c). In contrast, a semielliptical trajectory with $\theta = -0.26\pi$ gives a low rotary speed when $\Gamma=1/3$ and reaches the maximum speed when $\Gamma=0.486$, as shown in Fig. 6(d).

In the period 2 region $0.486 < \Gamma < 0.531$, Eq. (16) no longer applies as the steady-state orbit alternates between two collision states: the large-$|w_A|$ branch with a decreasing τ_{imp}, and the small-$|w_A|$ branch with an increasing τ_{imp} [see Fig. 6(b)]. Since $\dot{\beta}(t_{\mathrm{imp}})$ of the large-$|w_A|$ branch has a greater influence on the disk's steady-state rotational speed, as τ_{imp} shifts toward zero on the large-$|w_A|$ branch, the average rotational speed rises for Fig. 6(c) and falls for Fig. 6(d) until reaching the local extremum corresponding to the period 4 bifurcation.

As the disk visits an increasing number of points in the phase space (post period 4 bifurcation, and into the chaotic and chattering regime), the rotational dynamics of the disk is increasingly affected by Γ_T. For a large Γ_T, the rotary inertia of the disk dominates over the frictional torque, and the disk rotates at an average speed with small perturbations due to angular impulses $\hat{H}_n$ transferred at different times τ_{imp}. For a small Γ_T, however, the frictional torque dominates and the rotary speed of the disk oscillates wildly as the disk tracks $\dot{\beta}(t_{\mathrm{imp}})$ more closely. The effect of Γ_T on this oscillation of the speed can be seen by comparing Fig. 6(c) where $\Gamma_T=100$ and Fig. 6(d) where $\Gamma_T=1$. Note that the bifurcation diagram may appear to have three branches in what should be a period 4 region of Fig. 6(d). However, this is caused by the one-dimensional projection of orbits that exist in three-dimensional space $(\tau_{\mathrm{imp}}, w_A, w_T)$.

Past SWUM researchers [7,13] have assumed that the rotor can be considered stationary relative to the stator, leading to the conclusion that contact always occurs as the stator reaches its maximum vertical displacement ($\tau \approx \pi/2$), and that an elliptical trajectory—such as shown in Fig. 2(a), with
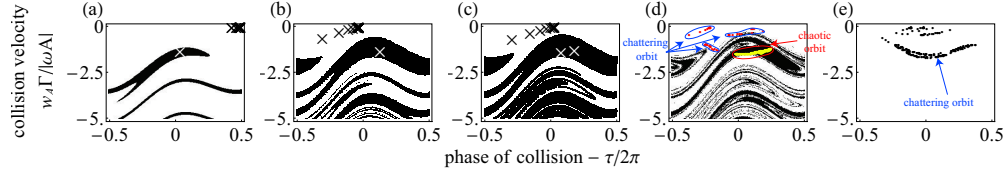
FIG. 7. (Color online) The basins of attraction for the following values of Γ: (a) 0.34, (b) 0.486, (c) 0.50, (d) 0.55, and (e) 0.60. The white regions are the basins of attraction of the chattering orbits [marked by black "$\times$"s in (a)–(c), red dots in (d), and black dots in (e)]. The black regions are the basins of attraction of the attractors that undergo the period doubling route to chaos [marked by white "$\times$" in (a)–(c) and yellow dots in (d)].

$\theta = -\tau_{\max} |\dot{\beta}| = -\pi/2$—is the optimal stator motion. We have shown, however, that when the vertical rotor motion is taken into account, the maximum steady-state rotational speed is achieved by choosing the right phase lag ($\theta = -\tau_{\mathrm{imp}}$) for a given Γ in the period 1 region ($0.333 < \Gamma < 0.486$). Contrary to the assumption of SWUM researchers, neither τ_{imp} is necessarily $\pi/2$ nor is elliptical motion the best stator trajectory.

B. Basins of attraction

We can see from the previous section that in order to achieve the maximum dough rotation speed, one should choose a hand motion within the period 1 regime ($0.333 < \Gamma < 0.486$) for multiple pizza tosses. We can further compare the relative "ease" at which a hand motion maintains dough rotation over multiple tosses by examining the effect of Γ on the basins of attraction; a larger basin of attraction implies that the orbit is more tolerant of variability in the hand motion. In Fig. 7, the basin of attraction of the period 1 orbit at $\Gamma = 0.34$ only covers 11.6% of the phase space shown; as Γ is increased, the basin of attraction widens to 39.1% of the phase space shown at $\Gamma = 0.486$. We can thus see that the use of semielliptical hand motion ($\theta = -0.26\pi$) with $\Gamma \approx 0.486$ has the advantage of being "easier" for maintaining the period 1 orbit required for maximum dough rotation speed.

The wide basins of attraction of the chattering orbits make them far easier to perform than period 1 multiple tosses. The fact that the $w_A = 0$ axis is deep within the basins of chattering orbits shows that period 1 orbits cannot be attained for a dough initially at rest if the tossing motion purely follows Eq. (1). This explains why dough-toss performers do not start multiple tosses with semielliptical hand motion right from the beginning, but instead employ a linear hand motion for the first few tosses.

Although it is unlikely that dough-toss performers will need to consult Fig. 6 and 7 to avoid chaotic and chattering orbits, the bifurcation diagrams and the basins of attraction provides SWUM researchers useful insights into the physical behavior of SWUMs. For example, SWUMs should be designed to operate away from the chaotic regime [e.g., $\Gamma = 0.55$ in Fig. 7(d)] because the extended region of the phase space visited by the disk reduces the rotor speed, and the fractal basin boundary of the attractors makes the motor behavior unpredictable. The maximum rotor speed ($\omega\Phi$) can be achieved in the period 1 regime, though complex control may be needed to actively adjust the stator motion to accommodate the evolving stator-rotor dynamics, since the basin of

attraction for period 1 orbits do not cover SWUM's usual initial condition. For $\Gamma > 0.561$, we see a sudden widening of the phase space explored by the orbits; the strange attractor of the chaotic orbits merges with the chattering orbit and the basin of attraction appears to fill the entire phase space [see Fig. 6(d)]. Although these orbits are eventually periodic, they differ from the low period chattering orbits in Figs. 7(a)–7(c): they have a longer period, and they follow the shadow of the chaotic strange attractor. SWUMs operated in this regime will not reach the maximum rotor speed, however, the wide basin of attraction suggests that they will operate most consistently. In Sec. V, our simulation results suggests that our prototype SWUM predominantly operates in this regime.

V. DYNAMICS OF SWUMS

The rotor and stator of our SWUM are, respectively, a 20-mm-diameter steel ball and a pretwisted beam that is glued to an axially poled piezoelectric transducer (see Fig. 8 for details of the geometry). By applying a sinusoidal electrical input to the transducer at a resonance frequency of the stator assembly, the stator tip is excited to vibrate with sufficient amplitude in the form described by Eq. (1) to induce rapid rotor rotation. Since the system's resonance frequencies are fixed by its geometry and material properties, the motor has two adjustable experimental parameters: the amplitude of the input voltage, altered via the use of a signal generator; and the rotor preload, altered by adjusting the distance between the steel ball and a magnet placed above it.
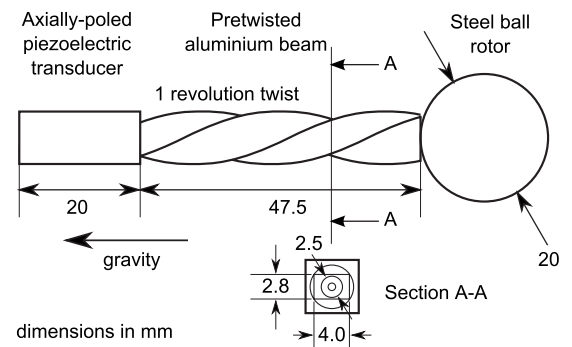

FIG. 8. Geometric details of our SWUM (not to scale). Note that this SWUM (Ref. [8]) is a simple prototype with preload provided by gravity.

TABLE III. Default values for the dimensional parameters

	Unknown				Known			
μ	ϵ	θ (rad)	A (m)	$\omega\Phi$ (rad/s)	a_e (mm)	a_g (mm)	ω (kHz)	g (m/s^2)
0.1	0.5	0	10^{-8}	30	1.25	6.3	70	10

A. Model parameters

In order to make direct comparisons between the SWUM and our model, we need to know the correspondence between the experimental conditions and the model parameters. A total of nine input parameters (a_g, a_e, ω, g, μ, ϵ, A, $\omega\Phi$, θ) are required to perform dimensional simulations, however, only four (a_g, a_e, ω, g) are accurately known: a_e and a_g depend on the design geometry of the SWUM, ω is set by the signal generator at a resonance frequency, and g can be adjusted and inferred from the measured weight of the motor setup. We thus compare the motor and the model indirectly by estimating the remaining parameters (μ, ϵ, A, $\omega\Phi$, θ) and using them as default values about which we study the sensitivity of the system to variations in the five parameters.

The default values of the parameters used in our simulations are shown in Table III; justifications for the values we selected for μ, ϵ, A, $\omega\Phi$, and θ are detailed below. We were unable to measure A, Φ, and θ during the motor's operation because the rotor blocks the access our instrumentation requires to the stator tip; the stator motion is thus estimated by measuring its vibration without the rotor, which shows that $A \sim 10^{-7}$ m and $\omega\Phi \sim 30$ rad/s. Assuming that the presence of the rotor decreases A more than $\omega\Phi$, we chose $A = 10^{-8}$ m as the default parameter while keeping $\omega\Phi = 30$ rad/s. The phase lag is assumed to be close to that of the free vibration of the stator, and thus we chose $\theta = 0$.

We estimated the coefficient of restitution ϵ by dropping a 20 mm steel ball from a height of 4.5 cm onto an aluminum beam sitting on a laboratory bench in a configuration similar to the motor; the resulting rebound height of 0.9 ± 0.5 cm implies $\epsilon = 0.4 \pm 0.1$ at an impact speed of 0.95 m/s. The coefficient of friction μ is estimated by measuring the rate at which the rotor decelerates ($\ddot{\alpha}_{\text{brake}}$) when power input to the motor is switched off [18]; in the absence of stator vibration, Eq. (2b) implies that

$$\mu = -\frac{ma_g^2\ddot{\alpha}_{\text{brake}}}{a_e N}. \quad (17)$$

The deceleration profiles were obtained for a range of preloads (see Fig. 9) giving us an average μ of 0.1 with a standard deviation of 0.06. Although reference values of μ between steel and aluminum under dry sliding conditions is about three times the results of our measurements (in the 0.3–0.4 range [19]), the difference may be explained by the fact that the stator and rotor are under line contact, which reduces the true contact area and correspondingly the coefficient of friction [20].
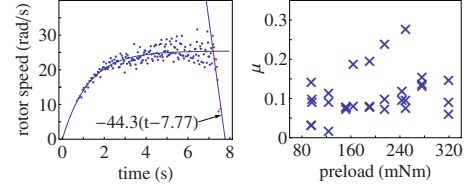

FIG. 9. (Color online) Determining the coefficient of friction between the rotor and the stator. A curve of the form $\dot{\alpha} = -\ddot{\alpha}_{\text{brake}}(t - t_c)$ is fitted to the deceleration profile when the motor is switched off; μ is then inferred from $\ddot{\alpha}_{\text{brake}}$ through Eq. (17). The right hand figure shows the measured μ at various preloads; in accordance with Coulomb friction, μ is relatively independent of preload and has an average of 0.10 and standard deviation of 0.06.

B. Comparison with experimental results

In Fig. 10, transient speed curves predicted by our model at the default parameter values (with A varied across its expected range), are shown next to measurements from three separate trials of our SWUM. The two sets of curves are qualitatively very similar: not only does our model predict the speed transients curves to be of the observed form ($\dot{\alpha}_{ss}(1 - e^{-t/t_c})$), it also accounts for the presence of what appears to be a high frequency, random oscillation that existing SWUM models have been unable to explain. In our model, the oscillation originates from the vertical rotor motion that is undergoing long period chattering (possibly with transient chaos), and is strongly affected by A: when A is small, collisions are more frequent and occur at lower speeds, leading
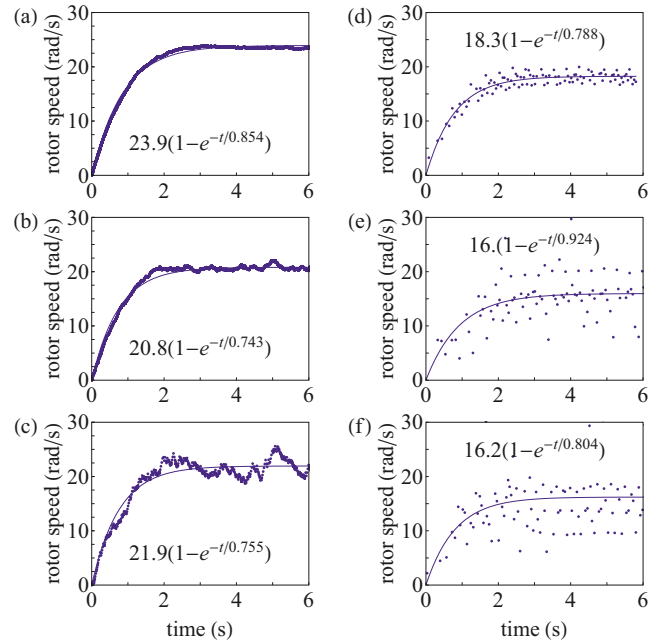

FIG. 10. (Color online) Transient speed curves each fitted with an equation of the form $\dot{\alpha}_{ss}(1 - e^{-t/t_c})$. (a)–(c) Simulation results at full preload for the following values of A: (a) 10^{-9} m, (b) 10^{-8} m, and (c) 10^{-7} m; all other parameters take on the default values in Table III. (d)–(f) Measured behavior of our SWUM at full preload and the same voltage input (0.55 V peak-to-peak) on three separate trials.
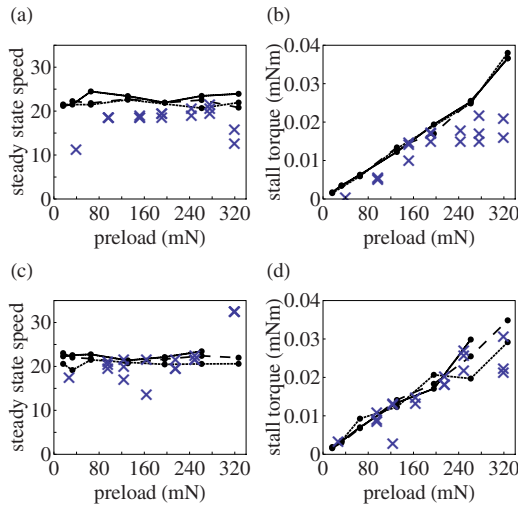
FIG. 11. (Color online) Effect of preload on steady-state speed and stall torque at two of the motor's operating frequencies: (a)–(b) $\omega = 70$ kHz with clockwise rotor rotation, and (c)–(d) $\omega = 184$ kHz with anticlockwise rotor rotation. The measured results are marked by crosses ($\times$) while the simulation results are marked by dots ($\bullet$) and joined to guide the eye. Points joined by solid, dashed, and dotted lines are, respectively, simulations performed at $A = 10^{-9}$, 10^{-8}, and 10^{-7} m.

to smoother transient speed curves; when A is large, infrequent high speed collisions results in large oscillations in rotor speed.

Quantitative comparisons are avoided since accurate values of five parameters are unknown; in fact our sensitivity study in the next section shows that the five parameters may be adjusted for a perfect match. We merely comment that reasonable values were chosen for our estimates and the resulting predictions are of the same order of magnitude as the measurements.

We thus focus on qualitative comparisons, and have found good agreement between the observed and predicted trends in steady-state speed and stall torque when preload is increased. In our model, the effects of preload are apparent in two ways: explicitly, through the parameter g, and implicitly, by modifying the stator motion. Except for the general expectation that the stator vibration amplitude will decrease when g is increased, A and $\omega\Phi$ and θ are unknown functions of g. We conjecture that A is more significantly affected by g than $\omega\Phi$ and θ, and thus in determining the effect of preload in our model, we varied g between 0.1 and 10 m/s^2 at three different axial vibration amplitudes, starting with $A = 10^{-7}$ m at low preloads and reducing to 10^{-8} and 10^{-9} m in the presence of preload (the default values were used for $\omega\Phi$ and θ).

Our experimental study [8] of SWUMs showed that for a large range of preloads between 80 and 280 mNm, the stall torque is proportional to preload, while the steady-state speed is relatively independent of preload. We can see from Fig. 11, where we overlay the simulation results with the experimental data, that similar trends are predicted by our bouncing-disk model when preload is in the 80–280 mNm range. Note also that the response of our model at the default frequency $\omega = 70$ kHz and the second operating frequency

$\omega = 184$ kHz are both consistent with experimental observation, adding further support that our model has correctly captured the stator-rotor momentum transfer process.

However, there are some features of the SWUM that our simulations fail to reproduce: for the $\omega = 70$ kHz case, there is a sharp fall in steady-state speed at low and high preloads, and the plateau in the stall torque when preload is greater than 200 mNm; for the $\omega = 184$ kHz case, there is a sharp rise in steady-state speed at high preloads. The discrepancies at high preload may be caused by the following: first, $\omega\Phi$ would be reduced as the preload is increased due to the suppression of stator axial vibration and therefore torsional vibration through the coupling mechanism within the twisted stator structure—this could explain the drop in steady-state speed at high preload when $\omega = 70$ kHz; and second, a qualitative change in the motor's dynamics can occur at high preload if A is reduced such that $\Gamma < 1/\pi$, in which case the stator acceleration would be insufficient for the stator-rotor separation to occur, and the rotor would no longer be "bouncing." The differences at low preload may be caused by the assumption that g is constant in our model, which may be valid when the axial motion of the rotor is small relative to its distance to the magnet used to adjust the preload, but fails as the magnet is drawn close to the rotor to achieve a low preload.

C. Predicted behavior of SWUMs

When the transient speed curves are of the form $\dot{\alpha}_{ss}(1 - e^{-t/t_c})$, we can compare simulated and observed results by their steady-state speed $\dot{\alpha}_{ss}$ and the stall torque $\dot{\alpha}_{ss}/t_c$. Note, however, that this transient response occurs in our bouncing-disk model when the vertical motion of the rotor undergoes long period chattering that traces the shadow of a chaotic strange attractor; for different parameters, the bouncing-disk system may undergo periodic or low period chattering orbits that give rise to qualitatively very different speed trajectories. Figure 12 shows an example of the speed trajectory that results from a low period chattering orbit: the periodic nature of the of orbit causes the angular momentum transfer to occur in a regular pattern, resulting in the linear rise in rotational speed. The angular impulse is limited by the relative angular speed of collision; thus when the rotor reaches the rotary speed of the stator at impact, there is an abrupt transition from the apparent constant acceleration to steady-state rotation. Note also that the speed trajectory appears to form multiple lines as the rotor cycles through collisions with different impact speeds.

So far, piecewise linear transient speed curves of this form have not yet been observed in SWUMs. We suspect that real motors operate in a region of the parameter space where low period chattering orbits are uncommon, and that they may be reproduced experimentally under the right conditions. This leads us to the results of our sensitivity study of the five parameters with estimated default values, where we found that the coefficient of restitution ϵ appears to have a strong effect on the presence of low period chattering orbits.

We varied each of the parameters μ, ϵ, A, $\omega\Phi$, and θ individually over their expected range while keeping all
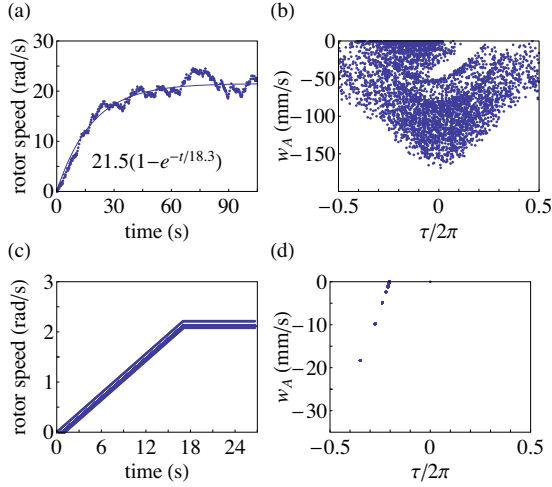
FIG. 12. (Color online) Comparison of the simulated transient speed curves when the rotor's vertical displacement undergoes long period and low period chattering orbits. The default model parameters in Table III are used except for: (a)–(b) $A=10^{-7}$ m and g =0.5 m/s^2 in the long period chattering case, and (d)–(e) A =10^{-8} m and $g=1$ m/s^2 in the low period chattering case.

other parameters at their default values. The predicted effect of each parameter on the steady-state speed and stall torque are shown in Fig. 13. Most of our simulations yielded transient speed curves of the form $\dot{\alpha}_{ss}(1-e^{-t/t_c})$, however, when $\epsilon<0.5$, low period chattering becomes the prevalent behavior of our model. With our ϵ estimated to be 0.4 ± 0.1 at 0.95 m/s and theories predicting ϵ to rise as collision speed is decreased [21], this may explain why low period chattering orbits have not been observed experimentally and suggests we should reduce ϵ in attempting to reproduce these orbits in SWUMs.

While the chief purpose of our sensitivity study is to determine the likely effect of errors in our estimated parameters, it also provides predictions that may be used for future comparisons with SWUMs and suggests which parameters are important for improving the motor. From Fig. 13, we can see that an error in some of the parameters will have a greater significance than the others; for example, the steady-state speed is most sensitive to θ, ϵ, and $\omega\Phi$, while the stall torque is most sensitive to θ, ϵ, and μ. Note that θ and ϵ appear to be the only two parameters that significantly affect both steady-state speed and stall torque; their effects are, however, limited to reducing steady-state speed and stall torque from the maximum values that are set, respectively, by $\omega\Phi$ and μ.
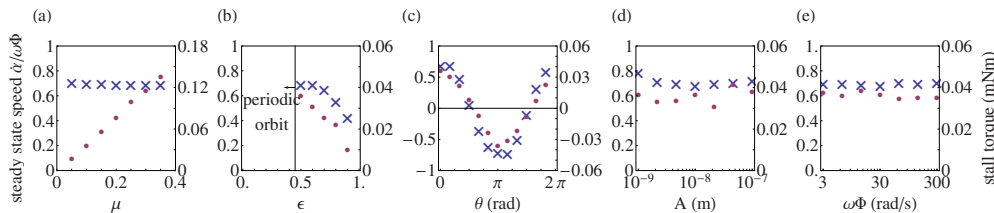
We have seen from Fig. 10 that A has a strong effect on the oscillation of the speed-time curve, thus it may seem curious that the steady-state speed and stall torque are not affected significantly by A even when it is varied by two orders of magnitude. A possible explanation for this is that the increased angular impulse $\hat{H}$ caused by larger collision speed w_A is offset by the longer interval between collisions ΔT

$$\hat{H} \sim \mu(1+\epsilon)w_A \quad \text{and} \quad \Delta T \sim w_A/g$$

implies $\hat{H}/\Delta T(\text{torque}) \sim \mu g(1+\epsilon)$.

Although the above argument also seems to explain the independence of stall torque to $\omega\Phi$, and the linear relationship between μ and the stall torque, it should be noted that this simplistic argument neglects the fact that collisions occur over a range of phases and speeds, and ultimately fails to correctly predict the effect of ϵ.

Consideration of how the collisions of the orbit are distributed in the state space (phase space) is needed for explaining the effects of θ and ϵ. The results for θ corresponds to a cosine curve because the collisions are more concentrated at $\tau\approx0$, thus the momentum transfer occurs predominantly when the angular velocity of the stator is $\dot{\beta}$ =$\omega\Phi\cos(\theta)$. The collisions are less concentrated at $\tau=0$ when ϵ is increased, thus leading to the decrease in both steady-state speed and stall torque.

VI. CONCLUSIONS

Pizza tossing and SWUMs share a common mechanism for converting reciprocating input into continuous rotary motion, and the physical behavior of both may be represented by the convenient adaptation of the bouncing ball model [2,3] to include rotation. Key features of the motion transfer process such as impact, separation and stick-slip frictional torque are captured by our bouncing-disk model, giving us a better understanding of SWUMs and pizza tossing. While there are many factors influencing the choice of tossing motion that we did not consider in detail, our bouncing-disk model shows that aspects of the tossing motion employed in the two basic pizza tossing modes do optimize certain performance measures: the linear trajectory used in single tosses maximizes rotation speed and efficiency, while the semielliptical motion used in multiple tosses maximizes the ease of maintaining the dough in the period 1 orbit that is required

FIG. 13. (Color online) Effect of varying (a) μ, (b) ϵ, (c) θ, (d) A, and (e) $\omega\Phi$ about the default parameter values. In each plot, the steady-state speed predictions are denoted by crosses ($\times$) with scales on the left hand frame, while the stall torque predictions are denoted by dots ($\bullet$) with scales on the right hand frame. Note that the rotor speed is nondimensionalized with respect to $\omega\Phi$.

for maximum steady-state speed. We applied our bouncing-disk model to our SWUM, using estimated parameters, and found that it reproduces the oscillations that have been observed in the motor's transient speed curves and have not been explained by existing models. Additionally, the predicted effect of preload on the steady-state speed and stall torque agrees with experimental observation.

APPENDIX: NEGLECTING DOUGH DEFORMATION

In the bouncing-disk model, the effects of dough deformation during the impact and contact phase of pizza tossing may be modeled with an appropriate choice of friction coefficient μ and coefficient of restitution ϵ. What is not modeled is the change in dough geometry, which causes changes to the moment of inertia and aerodynamic forces. However, as we will show below with data extracted from videos of pizza tossing, the change per toss in dough diameter is relatively small, thus the essential character of the process is the same as the bouncing-disk system.

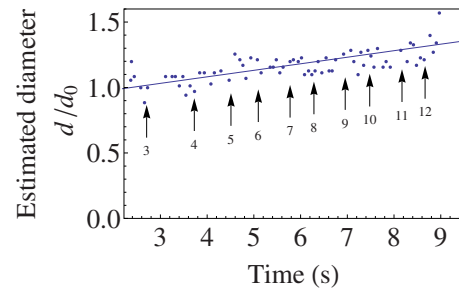A frame by frame diameter estimate of the dough in the multiple-toss video [11] (starting from the end of the second

FIG. 14. (Color online) Frame by frame estimate of dough diameter from the video of the mutliple-toss (Ref. [11]). The equation for the least-squares best fit is $d/d_0 = 1 + 0.0499(t - 2.365)$. The start of the nth toss is marked with an arrow.

toss at $t = 2.365$ s) is shown in Fig. 14; the diameter was measured in arbitrary units, fitted with a least-squares best fit, and finally the diameter was normalized with respect to the best fit diameter d_0 at $t = 2.365$ s. The start of each toss is marked with an arrow. From $n = 3$ to $n = 12$ the diameter grew by 30%, which is an average of 3% per toss.

[1] P. Pierański, Phys. Rev. A **37**, 1782 (1988).
[2] N. B. Tufillaro, Phys. Rev. E **50**, 4509 (1994).
[3] J. M. Luck and A. Mehta, Phys. Rev. E **48**, 3988 (1993).
[4] J.-C. Géminard and C. Laroche, Phys. Rev. E **68**, 031305 (2003).
[5] K. Szymanski and Y. Labaye, Phys. Rev. E **59**, 2863 (1999).
[6] N. B. Tufillaro and A. M. Albano, Am. J. Phys. **54**, 939 (1986).
[7] K. Nakamura, M. Kurosawa, and S. Ueha, IEEE Trans. Ultrason. Ferroelectr. Freq. Control **40**, 395 (1993).
[8] D. Wajchman, K.-C. Liu, J. Friend, and L. Yeo, IEEE Trans. Ultrason. Ferroelectr. Freq. Control **55**, 832 (2008).
[9] B. Watson, J. Friend, and L. Yeo, Journal of Micromechanics and Microengineering **19**, 022001 (2009).
[10] Video footage of single pizza tosses performed by Noah Elhage, captured on 3 October, 2007, camera operated by Kuang-Chen Liu.
[11] Online videos of multiple-toss, accessed 29 April, 2008 (http://www.throwdough.com/trick_basictoss.htm and http://www.youtube.com/watch?v=fAW0aDWaiSI).

[12] K. Nakamura, M. Kurosawa, and S. Ueha, IEEE Trans. Ultrason. Ferroelectr. Freq. Control **38**, 188 (1991).
[13] J. Guo, S. Gong, H. Guo, X. Liu, and K. Ji, IEEE Trans. Ultrason. Ferroelectr. Freq. Control **51**, 387 (2004).
[14] J. Tsujino, Smart Mater. Struct. **7**, 345 (1998).
[15] K.-C. Liu, J. Friend, and L. Yeo, EPL **85**, 60002 (2009).
[16] H. L. Nusse and J. A. Yorke, *Dynamics: Numerical Explorations* (Springer-Verlag, Berlin, 1994).
[17] J. P. Laraudogoitia, in *The Stanford Encyclopedia of Philosophy*, edited by E. N. Zalta (Stanford University, Palo Alto, CA, 2008).
[18] K. Nakamura, M. Kurosawa, H. Kurebayashi, and S. Ueha, IEEE Trans. Ultrason. Ferroelectr. Freq. Control **38**, 481 (1991).
[19] *CRC Handbook of Engineering Tables*, edited by R. C. Dorf (CRC Press, Boca Raton, FL, 2004).
[20] shppE.-S. Yoon, R. A. Singh, H.-J. Oh, and H. Kong, Wear **259**, 1424 (2005).
[21] G. Kuwabara and K. Kono, Jpn. J. Appl. Phys. **26**, 1230 (1987).